

# A 3D Polar Processing Algorithm for Scale Model UHF ISAR Imaging

Christopher J. Beaudoin<sup>\*a</sup>, Andrew J. Gatesman<sup>a</sup>, Robert H. Giles<sup>a</sup>, Jerry Waldman<sup>a</sup>, and William E. Nixon<sup>b</sup>

<sup>a</sup>Submillimeter-Wave Technology Laboratory, University of Massachusetts Lowell,  
Lowell, MA 01854

<sup>b</sup>U.S. Army National Ground Intelligence Center, 2055 Boulders Road,  
Charlottesville, VA 22911-8318

## ABSTRACT

In recent years, UHF synthetic aperture radar has become a growing area of interest among the radar community. Due to their relatively long wavelengths, UHF systems provide advantages that may not be attainable by microwave and millimeter-wave radar systems. These advantages include excellent target detection statistics in high clutter environments, wide-area surveillance, and long stand-off ranges. UHF systems also have proven synergistic properties with higher frequency radar systems in applications such as topographical mapping. However, the ability to study the characteristics of these lower frequency radar systems in a controlled and systematic environment is difficult. In this work, a physical scale modeling process is utilized to generate three-dimensional UHF imagery that may be used to study scattering phenomenology at these wavelengths. Dimensionally and dielectrically scaled targets and scenes are measured in a 6 – 18 GHz microwave compact range to model the backscatter of the full-size target at UHF wavelengths. The microwave compact radar range and transceiver hardware utilized to model UHF radar signature data are briefly described. A description of the image processor used to generate three-dimensional UHF imagery from wide-band/wide-angle data collections is described as well. Finally, imagery of radar signature data collected from a M1A1 Abrams main battle tank model is examined. The high resolution imagery resulting from the wide-band/wide-angle collection will show that sub-wavelength features of ground targets are resolvable at these wavelengths.

**Keywords:** UHF, 3D ISAR, radar, scale-modeling

## 1. INTRODUCTION

### 1.1 Applications of UHF SAR

In the past 15 years, there has been a renewed interest in UHF SAR among the radar community for various problems where high frequency sensors do not provide an adequate solution. Due to their relatively long wavelengths, UHF signals can penetrate optically-dense materials much more effectively than those of sensors operating at shorter wavelengths. This property makes UHF SAR suitable for detecting targets beneath a foliage canopy, which has been coined the Foliage PENetration (FOPEN) problem.<sup>1</sup> Such sensors are also capable of Ground PENetration (GPEN), thereby allowing detection of sub-terrain objects.<sup>2</sup> Low frequency SAR also has demonstrated use in scene change detection.<sup>3</sup> This technique scrutinizes the temporal differences between two SAR images of an identical scene to determine what scattering centers have moved between the two collections. It has also been found that UHF change detection analysis is much less sensitive to natural temporal decorrelations of the scene (i.e. fluttering leaves and grass) than change detection analysis conducted at higher frequencies.<sup>3</sup> This characteristic makes UHF SAR change detection a much more robust tool in determining movement of vehicles as well as small man-made structures. Due to their wide-beamwidth, UHF SAR can provide wide-area surveillance and therefore can provide change information over much larger area than can typically be scanned by a high frequency SAR.<sup>3,4</sup> Furthermore, due to its penetration capabilities, UHF systems can provide change information about targets beneath foliage and sub-terrain objects.<sup>4,5</sup> Radar test beds have also been developed to exploit the synergies between UHF and X-band SAR sensors.<sup>6</sup> When used together in an interferometric modality, the sensors can provide a thorough topological mapping of a forested area. Because of its penetration capabilities, UHF SAR is used to map the topology below the foliage canopy. The X-band SAR sensor, unable to penetrate the foliage canopy, is used to map the topology of the canopy itself.

<sup>\*</sup>correspondence: email: christopher\_beaudoin@uml.edu; telephone: 978-934-1366; fax: 978-452-3333; web: <http://stl.uml.edu>;  
mail: Submillimeter-Wave Technology Laboratory, 175 Cabot Street, Suite 130, Lowell, MA 01854

Report Documentation Page				Form Approved OMB No. 0704-0188	
Public reporting burden for the collection of information is estimated to average 1 hour per response, including the time for reviewing instructions, searching existing data sources, gathering and maintaining the data needed, and completing and reviewing the collection of information. Send comments regarding this burden estimate or any other aspect of this collection of information, including suggestions for reducing this burden, to Washington Headquarters Services, Directorate for Information Operations and Reports, 1215 Jefferson Davis Highway, Suite 1204, Arlington VA 22202-4302. Respondents should be aware that notwithstanding any other provision of law, no person shall be subject to a penalty for failing to comply with a collection of information if it does not display a currently valid OMB control number.					
1. REPORT DATE <b>MAY 2006</b>		2. REPORT TYPE		3. DATES COVERED <b>00-00-2006 to 00-00-2006</b>	
4. TITLE AND SUBTITLE <b>A 3D Polar Processing Algorithm for Scale Model UHF ISAR Imaging</b>				5a. CONTRACT NUMBER	
				5b. GRANT NUMBER	
				5c. PROGRAM ELEMENT NUMBER	
6. AUTHOR(S)				5d. PROJECT NUMBER	
				5e. TASK NUMBER	
				5f. WORK UNIT NUMBER	
7. PERFORMING ORGANIZATION NAME(S) AND ADDRESS(ES) <b>University of Massachusetts Lowell, Submillimeter-Wave Technology Laboratory, 175 Cabot Street, Lowell, MA, 01854</b>				8. PERFORMING ORGANIZATION REPORT NUMBER	
9. SPONSORING/MONITORING AGENCY NAME(S) AND ADDRESS(ES)				10. SPONSOR/MONITOR'S ACRONYM(S)	
				11. SPONSOR/MONITOR'S REPORT NUMBER(S)	
12. DISTRIBUTION/AVAILABILITY STATEMENT <b>Approved for public release; distribution unlimited</b>					
13. SUPPLEMENTARY NOTES <b>The original document contains color images.</b>					
14. ABSTRACT					
15. SUBJECT TERMS					
16. SECURITY CLASSIFICATION OF:			17. LIMITATION OF ABSTRACT	18. NUMBER OF PAGES <b>11</b>	19a. NAME OF RESPONSIBLE PERSON
a. REPORT <b>unclassified</b>	b. ABSTRACT <b>unclassified</b>	c. THIS PAGE <b>unclassified</b>			

The development of stealth technology has also contributed to the trend in the renewed interest of low frequency radars. Low RCS objects typically exhibit an RCS proportional to the square of the wavelength. This property is attributed to resonant effects at these long wavelengths because the target sizes are typically on the order of the radar wavelength. Therefore, longer wavelength radars have a better probability of detecting stealthy targets.<sup>7</sup>

### **1.2 Need for UHF Radar Measurement Capability**

Due to the renewed interest in UHF radar research, a need for high quality, calibrated UHF radar data exists. Airborne operational UHF radar systems are currently in use; however, such systems must contend with less than ideal operating conditions. Such examples of these non-ideal conditions are unknown flight path deviations, uncorrected systematic errors in the calibration process, and radio frequency interference (RFI). Furthermore, the conditions required for a particular study may not be available or feasible. Therefore, such operational radar systems may not be capable of conducting a controlled and systematic study of a particular problem. Radar automatic target recognition (ATR) developers rely on very accurate SAR imagery of targets in order to train identification algorithms.<sup>8</sup> Ideally, an entire imagery library of the target in a variety of orientations and articulations would be available in order to train the algorithm on any possible circumstance in which the radar may observe the target. Training an ATR algorithm on such a library of imagery maximizes the likelihood of correctly classifying a given unknown target. Radar signature libraries of targets do exist for microwave and millimeter-wave radar systems; however, the available radar signature libraries at UHF frequencies are limited.

As noted earlier, a major problem faced by operational UHF SAR systems is the issue of radio frequency interference.<sup>9</sup> The sources of the unwanted signals are typically radio and television stations with which the radar must share bandwidth. Operational UHF systems must contend with these unwanted signals and as a result, the available sets of data are said to be sparse-band.<sup>20</sup> These sparse-bands of data create issues in SAR imagery in terms of increasing image side-lobe levels<sup>20</sup>, while the RFI signals introduce spurious scatterers in the imagery.<sup>10</sup> RFI suppression is currently a topic of active research to mitigate these spurious signals and the availability of data not corrupted by such signals may assist in developing practical methods.

### **1.3 Physical Scale Modeling Approach to UHF Radar Data Collections**

Since 1981, Expert Radar Signature Solutions (ERADS) under funding from the National Ground Intelligence Center (NGIC) has developed state-of-the-art scale model measurement systems to acquire radar signatures in support of a number of advanced radar applications such as automatic target recognition (ATR) systems, RAM development, and buried object detection. ERADS has developed compact ranges at 12 GHz<sup>11</sup>, 160 GHz<sup>12</sup>, 520 GHz<sup>13</sup>, and 1.56 THz<sup>14</sup> for acquisition of UHF, X-band, Ka-band, and W-band radar imagery of, 1/16<sup>th</sup>, 1/35<sup>th</sup> and 1/48<sup>th</sup> scale model targets and scenes.

Radar scale modeling requires that the target's geometric and dielectric properties be scaled appropriately. Therefore, the complex dielectric constant of any nonmetallic component of the full scale target at the full scale wavelength must be matched to the complex dielectric constant of the corresponding scale model component at the scaled wavelength. The University of Massachusetts Lowell Submillimeter-Wave Technology Laboratory (STL) has demonstrated the technology necessary to tailor the dielectric properties of materials.<sup>15,16</sup> Conductive coatings necessary to simulate the metallic body and components of the full scale vehicles have been developed as well.

## **2. METHODOLOGY**

### **2.1 3D UHF Radar Data Collection Process**

A 6-18 GHz compact range (depicted in figure 1a) was utilized to collect target radar signatures in the scale-model environment. The radar system operates in a stepped-frequency, pulsed/CW modality and incorporates a large off-axis parabolic reflector to emulate far-field target illumination and monostatic backscatter collection. The reflector is capable of illuminating a 2 ft. by 2ft. by 2ft. volume with uniform planar wavefronts. Currently, the system operates in the linear HH and VV polarization channels with a planned upgrade to polarimetric measurement capability.

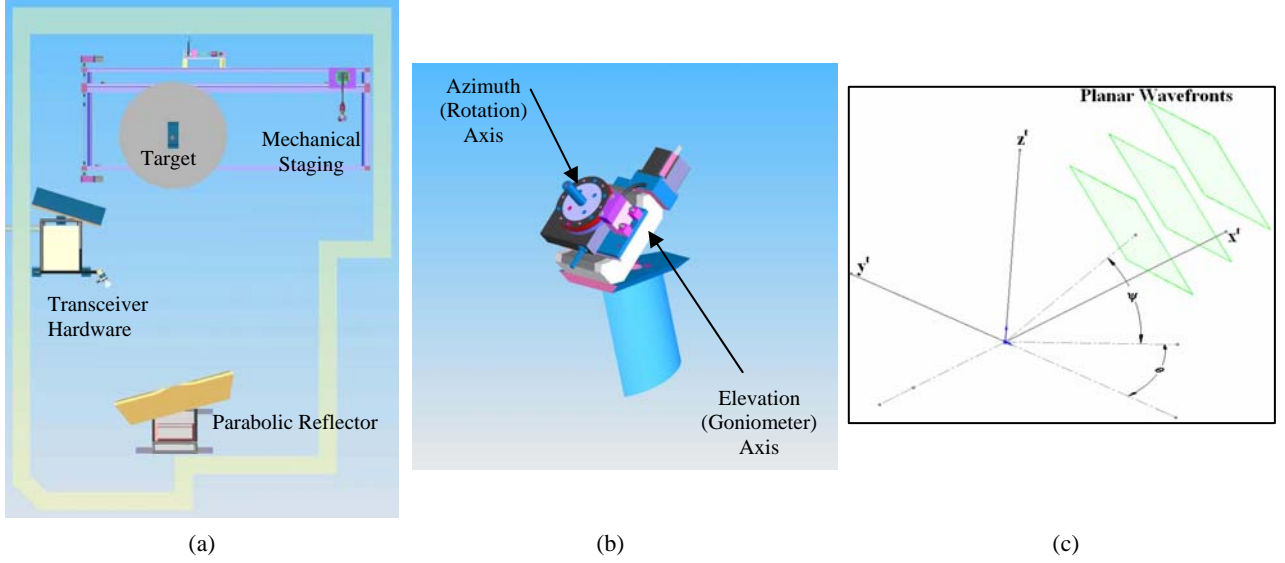


Figure 1: Data collection methodology (a) microwave compact radar range (b) 2D Az-El target scanning stage (c) data collection geometry.

Furthermore, the compact radar range incorporates a 2D azimuth-elevation (Az-El) mechanical scanning stage (shown in figure 1b) which is used to orient a free-space 1/35<sup>th</sup> scale target at a variety of angles.

The UHF data collection system samples the target's complex backscatter phasor,  $\Phi$ , at every frequency step, over a specified range of azimuth and elevation illumination angles, thereby providing three-dimensional data collections. The data collection sample arrays are defined by the following:

$$f(p) = f_c - \frac{f_b}{2} + p\Delta_f \quad p = 0, 1, 2, \dots, \frac{f_b}{\Delta_f} - 1 \quad (1a)$$

$$\theta(q) = \theta_c - \frac{\theta_a}{2} + q\Delta_\theta \quad q = 0, 1, 2, \dots, \frac{\theta_a}{\Delta_\theta} - 1 \quad (1b)$$

$$\psi(s) = \psi_c - \frac{\psi_a}{2} + s\Delta_\psi \quad s = 0, 1, 2, \dots, \frac{\psi_a}{\Delta_\psi} - 1 \quad (1c)$$

Equation (1) defines the sample arrays specifying the frequency, azimuth, and elevation locations  $f(p)$ ,  $\theta(q)$ , and  $\psi(s)$ , respectively, at which the target's backscatter phasor  $\Phi(f, \theta, \psi)$  is sampled during the data collection process. The parameters  $f_b$ ,  $\theta_a$ , and  $\psi_a$  represent the total span of the 3D data collection in frequency, azimuth, and elevation angle, respectively, while  $f_c$ ,  $\theta_c$ , and  $\psi_c$  represent the center frequency, azimuth, and elevation angles of the aperture. The uniform sample increments in frequency, azimuth, and elevation angle are given by  $\Delta_f$ ,  $\Delta_\theta$ , and  $\Delta_\psi$ , respectively, while  $p$ ,  $q$ , and  $s$  are the sample indices of the respective dimensions. The parameters  $f_b$ ,  $\theta_a$ ,  $\psi_a$ ,  $f_c$ ,  $\theta_c$ ,  $\psi_c$ ,  $\Delta_f$ ,  $\Delta_\theta$ , and  $\Delta_\psi$  are referred to as the data collection parameters and the collection of  $\Phi(f, \theta, \psi)$  is referred to as the radar signature data. The  $(x^t, y^t, z^t)$  coordinate system shown in figure 1c is referred to as the target-fixed system as it defines the coordinate geometry that is fixed to the body of the target under measurement.

## 2.2 Wide-Band/Wide-Angle 3D ISAR Image Formation Processor

The polar format algorithm (PFA) is used here to develop the 3D image formation processor in which the radar signature data are processed. The PFA has been applied widely for use in monostatic SAR imaging of instrumented and operational data collections.<sup>17,18</sup> In essence, the algorithm provides an elegant technique of formatting coherent radar data collected under plane wave illumination over a wide angular aperture such that they may be interpreted as the spatial Fourier

transform of the target's 3D reflectivity distribution. After the appropriate formatting of the data, a multidimensional Fourier transform process is performed to provide a reconstruction of the target's reflectivity distribution. This method provides a geometrically accurate reconstruction (from the available data) of the target reflectivity distribution in the case when the incident wavefronts are planar across the breadth of the target and the backscattered wavefronts are sampled in the far-field. The compact radar range configuration utilized in the data collection process (shown in figure 1a) ensures that both requirements are satisfied. Based on the data collection diagram shown in figure 1c, the target-fixed spatial frequency locations of the samples of  $\Phi(f, \theta, \psi)$  can be represented as<sup>19</sup>:

$$\bar{F}'(p, q, s) = \begin{bmatrix} F_x'(p, q, s) \\ F_y'(p, q, s) \\ F_z'(p, s) \end{bmatrix} = 2k(p) \begin{bmatrix} -\sin(\theta(q))\cos(\psi(s)) \\ \cos(\theta(q))\cos(\psi(s)) \\ -\sin(\psi(s)) \end{bmatrix} \quad (2a)$$

$$k(p) = \frac{2\pi f(p)}{c} \quad (2b)$$

where  $\bar{F}'(p, q, s)$  is the Fourier space vector defining the location of the data sample at the target-fixed spatial frequency coordinates  $F_x'$ ,  $F_y'$ , and  $F_z'$ . The scalar  $k(p)$  is the wavenumber of the electromagnetic wave having frequency  $f(p)$ . The acquired radar signature data  $\Phi(f, \theta, \psi)$  are said to reside in a volume in 3D Fourier space (figure 2a).

In order to facilitate the ISAR image processing, the 3D polar process aperture shown in figure 2a is transformed from the target-fixed spatial frequency coordinates  $(F_x', F_y', F_z')$  to the radar-fixed spatial frequency coordinates  $(F_x, F_y, F_z)$ . The transformation maintains a fixed rotational orientation of the 3D process aperture in the  $(F_x, F_y, F_z)$  coordinate system, regardless of the center azimuth and elevation angles,  $\theta_c$  and  $\psi_c$ , thereby simplifying upcoming processing tasks. The coordinate transformation can be viewed as a 2D rotation of the 3D process aperture by the center azimuth and elevation angles,  $\theta_c$  and  $\psi_c$  and is given by the following:

$$\bar{F}(p, q, s) = \begin{bmatrix} F_x(p, q, s) \\ F_y(p, q, s) \\ F_z(p, q, s) \end{bmatrix} = 2k(p) \begin{bmatrix} -\cos(\psi(s))\sin(\theta(q) - \theta_c) \\ \sin(\psi(s))\sin(\psi_c) + \cos(\psi(s))\cos(\psi_c)\cos(\theta(q) - \theta_c) \\ -[\sin(\psi(s))\cos(\psi_c) - \cos(\psi(s))\sin(\psi_c)\cos(\theta(q) - \theta_c)] \end{bmatrix} \quad (3)$$

A diagram of the 3D process aperture in the radar-fixed spatial frequency coordinate system is shown in figure 2b. Ultimately, the rotation of the 3D process aperture causes the image reconstructions to revolve about the radar-fixed coordinate system in response to varying the center azimuth and elevation angles,  $\theta_c$  and  $\psi_c$ , of the 3D process aperture.<sup>17</sup> This is the so called inverse synthetic aperture radar (ISAR) processing modality (i.e. a fixed antenna illuminating a rotating target).

Application of a Fourier transform to the samples of the target's backscatter phasor  $\Phi(F_x, F_y, F_z)$  having locations described by equation (3) produces a reconstruction of the target's 3D reflectivity distribution. In the interest of computational efficiency, the ISAR image reconstruction process is carried out by first performing a 3D interpolation of the data samples onto a 3D Cartesian grid. A 3D fast Fourier transform (FFT) process is then applied to the interpolated samples to provide a reconstruction of the target's 3D reflectivity distribution.

### 2.2.1 3D Cartesian Grid Construction

As shown in figure 2b, the Cartesian grid (box) is circumscribed onto the available 3D process aperture such that the entire aperture is included within the grid. Determining the boundaries of the Cartesian volume is a matter of analyzing the 3D geometry of the situation depicted in figure 2b for an arbitrary set of  $f_b, f_c, \psi_a, \psi_c$ , and  $\theta_a$ . Because of the coordinate system transformation described by equation (3), a fixed rotational orientation of the 3D process aperture with respect to the  $(F_x, F_y, F_z)$  coordinate system is maintained, regardless of the data collection parameters. The boundaries of the Cartesian volume circumscribing the 3D process aperture are given by the quantities,  $F_{xmin}, F_{ymin}, F_{zmin}, F_{xmax}, F_{ymax}$ , and  $F_{zmax}$  and are determined through a geometrical analysis of figure 2b which is outside the scope of this paper. The 3D Cartesian sample

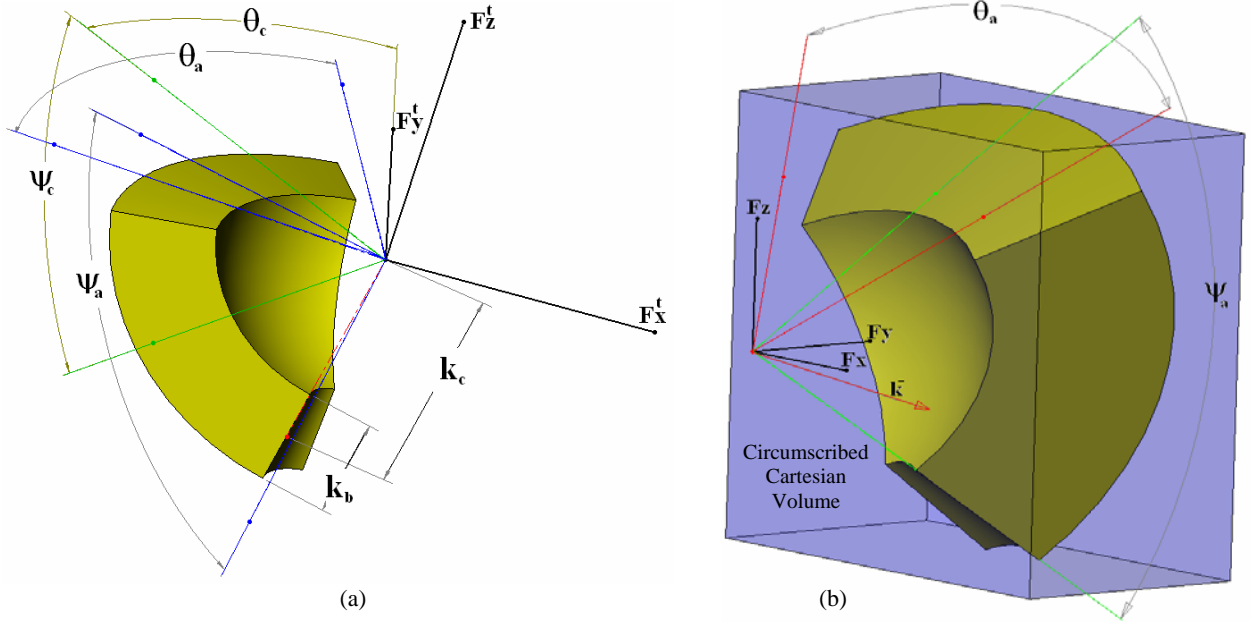


Figure 2: 3D polar process aperture in (a) target-fixed and (b) radar-fixed spatial frequency coordinates.

grid is then defined by set of arrays describing the sample locations in the  $F_x$ ,  $F_y$  and  $F_z$  dimensions limited by the boundaries in the respective dimensions. The  $F_x$ ,  $F_y$ , and  $F_z$  3D Cartesian grid sample locations are given by:

$$F_{xc}(u) = F_{x \min} + u\Delta_{Fx} \quad u = 0, 1, 2, \dots, \frac{F_{x \max} - F_{x \min}}{\Delta_{Fx}} - 1 \quad (4a)$$

$$F_{yc}(v) = F_{y \min} + v\Delta_{Fy} \quad v = 0, 1, 2, \dots, \frac{F_{y \max} - F_{y \min}}{\Delta_{Fy}} - 1 \quad (4b)$$

$$F_{zc}(w) = F_{z \min} + w\Delta_{Fz} \quad w = 0, 1, 2, \dots, \frac{F_{z \max} - F_{z \min}}{\Delta_{Fz}} - 1 \quad (4c)$$

In equation (5),  $F_{xc}(u)$ ,  $F_{yc}(v)$  and  $F_{zc}(w)$  are the 3D Cartesian grid sample locations in the  $F_x$ ,  $F_y$ , and  $F_z$  dimensions, respectively, while  $\Delta_{Fx}$ ,  $\Delta_{Fy}$ , and  $\Delta_{Fz}$  symbolize the sample intervals and  $u$ ,  $v$ , and  $w$  are the sample location indices of the respective dimensions. In order to preserve the spectral content of the polar formatted samples in the Cartesian grid, the sample intervals  $\Delta_{Fx}$ ,  $\Delta_{Fy}$ , and  $\Delta_{Fz}$  are determined by the data collection sample increments  $\Delta_f$ ,  $\Delta_\theta$  and  $\Delta_\psi$  as given by:

$$\Delta_{Fx} = \frac{2\pi f^+ \Delta_\theta}{c} \quad (5a)$$

$$\Delta_{Fy} = \frac{4\pi \Delta_f}{c} \quad (5b)$$

$$\Delta_{Fz} = \frac{2\pi f^+ \Delta_\psi}{c} \quad (5c)$$

where  $f^+$  is the maximum frequency at which data are collected as is determined by equation 1a.

### 2.2.2 3D Interpolation Process

The 3D interpolation method developed in this work implements a one-dimensional *sinc* function interpolator<sup>17</sup> in the three separate spatial frequency dimensions to generate samples on the circumscribed 3D Cartesian grid defined by equation (5). Analysis of equation (3) reveals that the 3D process aperture may be decomposed into individual elevation-cut planes (i.e. data collected at fixed  $\theta(\mathbf{q})$ ) in each of which the samples lie on a polar raster. Two-dimensional interpolation of polar raster samples onto a rectangular grid in conjunction with the PFA has been described in the literature.<sup>17</sup> For a given elevation-cut plane, the data samples are first interpolated along the wavenumber lines (i.e. fixed  $\psi(s)$  and  $\theta(\mathbf{q})$ ) to obtain output samples located at the desired  $F_y$  locations given by equation (5b). The samples produced by the  $F_y$  interpolation are then interpolated along the  $F_z$  direction (i.e. fixed  $F_{yc}(\mathbf{u})$  and  $\theta(\mathbf{q})$ ). The result of this  $F_z$  interpolation positions the output samples at the desired  $F_z$  locations given by equation (5c). This 2D interpolation process is repeated in each elevation cut plane. The final  $F_x$  interpolation is performed at each  $(F_{yc}(\mathbf{u}), F_{zc}(\mathbf{w}))$  coordinate in the Cartesian grid and places samples between the adjacent elevation-cut planes such that they are located at the desired  $F_x$  locations given by equation (5a). The 3D array of samples resulting from the  $F_x$  interpolation are then co-located with the 3D Cartesian grid.

## 3. RESULTS

3D radar signature data were collected on the 1/35<sup>th</sup> scale model M1A1 Abrams main battle tank shown in figure 3. The M1A1 Abrams model is configured in the travel-mode (transport) position, and is affixed with Identification Friend or Foe (IFF) panels. The data were collected in the VV polarization channel with frequency parameters  $f_c = f_b = 342$  MHz, and  $\Delta f = 3.43$  MHz over a 360° span in azimuth angle  $\theta$ , with  $\psi_c = 45^\circ$ ,  $\psi_a = 72^\circ$ , and  $\Delta\theta = \Delta\psi = 2^\circ$ . 3D UHF ISAR imagery was generated from the radar signature data collection utilizing the wide-band/wide-angle 3D ISAR image formation processor described in section 2.2. Figures 4 and 5 display several projections of the 3D UHF imagery generated from the M1A1 Abrams radar signature collection. The data were processed over the full radar bandwidth and elevation aperture with  $\psi_c = 45^\circ$  and utilized an azimuth aperture  $\theta_a = 72^\circ$  at  $\theta_c = 120^\circ$  (figure 4) and  $\theta_c = 180^\circ$  (figure 5) to form the imagery. Based on the processing parameters, the peak to null mainlobe width of the wide-band/wide-angle imaging system's impulse response function<sup>18</sup> is 0.44 meters in the range dimension and 0.37 meters in cross-range and height dimensions. The ISAR imagery shown in figures 4 and 5, therefore, exhibit 0.44 meter range resolution and 0.37 meter cross-range and height resolution. We note here that the data are collected over a wavelength span of 0.58 – 1.75 meters. In figures 4 and 5, the positive cross-range (x) axis is shown in red, positive range (y) axis in white, and positive height (z) axis in blue. Also note that the radar propagates in the direction of the positive y axis in the radar-fixed coordinate system. As such, the x-z projection represents the front aspect view of the 3D ISAR image at azimuth/elevation view angle = 0°, the y-z projection represents the side aspect view at azimuth view angle = 90°, elevation view angle = 0°, while the x-y projection represents the top aspect view at azimuth view angle = 0° and elevation view angle = 90°. Figures 4d and 5d display arbitrary views of the imagery at the aspect angles captioned in the respective figures.

The imagery in figures 4 and 5 differ somewhat from traditional 2D ISAR imagery by the manner in which the image intensities are displayed. Because of the three-dimensional nature of the RCS intensity distributions which have been rendered to the two-dimensional images shown in figures 4 and 5, the peak of the scattering centers are masked by the three-dimensional ideal point scatterer image response (i.e. impulse response function of the system). One may visualize a constant intensity level in the imagery, encoded by constant color, as a surface which encompasses the higher intensity surfaces within. As such, the surfaces of constant intensity must be “peeled back” in order to reveal surfaces of higher intensity. The process of peeling back the constant intensity surfaces, however, has the unfortunate effect of reducing the image's overall dynamic range. Therefore, a trade-off must be made between display of the image's dynamic range and visualization of the scattering centers at the core of the imagery. For this reason, 8 dB (-18 → -10 dBsm) of dynamic range is shown in figures 4 and 5 in order to allow visualization of the target's main scattering features. The low level intensity in the imagery is represented by the color green which is succeeded by the colors yellow and orange then by the high level intensity signified by the color red. Through close scrutiny of the imagery, one may observe higher level colors behind the low level green surfaces.

Considering the relatively long wavelengths used in the 3D UHF ISAR imaging experiment, the imagery shown in figures 4 and 5 provide resolution sufficiently high enough to isolate individual scattering features contributing to the target's 3D reflectivity distribution. In comparing the ISAR imagery of figure 4 to the corresponding photo of the M1A1 at the equivalent azimuth view angle (figure 3a), various distinct physical features of the MBT can be associated to the scattering behavior shown in the imagery. As shown in figure 4, the high resolution imagery allows identification of the seven exposed

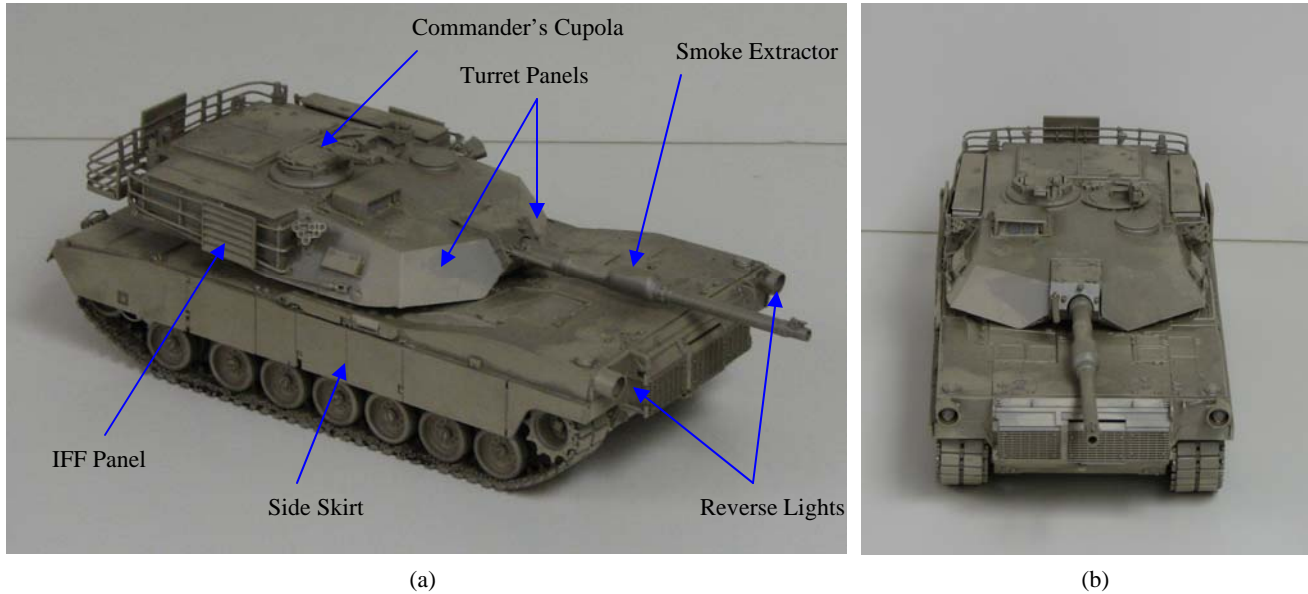


Figure 3: 1/35<sup>th</sup> scale model M1A1 Abrams MBT in travel mode with IFF panels at (a) 120° azimuth aspect and (b) 180° azimuth aspect poses as viewed by the radar during data collection

wheels of the tank, each of which has a 0.625 meter diameter. Furthermore, the imagery also reveals the asymmetric spacing of the rear wheel as observed in figure 3a. This feature is a main distinction between US and Russian-made MBT's. The two edges of the flat plate running lengthwise with the tank's body, formed by the side skirt shielding the wheels, are also resolved in the imagery. Because the scattered waves are redirected from the backscatter direction by the skirt's plate at this center azimuth/elevation angle, a shadow spanning the length of the skirt can be observed in figures 3a, 3b, and 3d between the two edges of the plate. Also shown in the imagery is a tapered elongation of this plate's top edge at the front of the tank in response to the corresponding structure shown in figure 3a. The small "plate-like" IFF panel affixed to the illuminated side of the tank's turret also generates a shadow in figures 4a, 4c and 4d. The illuminated panel on the front of the tank's turret also possesses a planar surface which appears brightly in the imagery. In this particular aspect view, the scattered waves from this surface are directed back toward the radar making the surface visible at this process aspect angle. The opposing panel of the turret appears as a shadow in the imagery as the scattered waves are primarily directed away from the radar. We also note that sub-wavelength features comprising the tank such as commander's cupola, the reverse lights, and the smoke extractor located in the center of the cannon's barrel are well-resolved in the imagery.

#### 4. SUMMARY AND CONCLUSIONS

The active role of the UHF SAR sensor in present-day remote sensing applications requires that such systems be studied in-depth in order to fully exploit the sensor's capabilities. In this work, we have used a 6-18 GHz scale model radar signature data collection system to generate UHF radar signature data on a free space tactical target. A 3D ISAR image formation processor used to reconstruct the 3D reflectivity distribution of a target from its radar signature data was also presented. Finally, high resolution 3D ISAR imagery generated from a freespace radar signature data collection of an M1A1 Abrams MBT demonstrated the feasibility of studying UHF SAR using the described radar scale-modeling and image processes.

Considering the electromagnetic scattering processes taking place during a wide-bandwidth, wide-angle radar signature data collection, it is conceivable that scatterer persistence through the entire data collection aperture may limit the resolution achievable by the imaging system. That is, the shorter the persistence of a given scatterer through the data collection process, the more coarsely that scatterer is resolved. The UHF ISAR imagery presented in this work demonstrates that high resolution can be attained in a long wavelength imaging system if wide-bandwidth, wide-aperture collections are

feasible. This outcome is most likely a result of the electromagnetic scattering regime in which the measurements takes place.

Because the wavelengths used in UHF SAR are on the order of the size of the target, the target and its features experience Rayleigh and resonance scattering phenomena. In this scattering regime, scattering amplitude is largely independent of illumination angle<sup>7</sup> and this being the case, scatterers tend to persist throughout the data collection aperture. Such a rationalization may explain why scatterer persistence does not limit the achievable resolution in the long-wavelength, wide-angle imaging scenario described in this work. In an attempt to validate this hypothesis, one may consider generating ISAR imagery from a radar data collection of the identical target in a short wavelength system where low frequency scattering phenomena are longer prevalent and analyze the relationship between scatterer resolution and the extent of the data collection aperture.

## ACKNOWLEDGEMENTS

The authors wish to thank Mr. Michael Coulombe and Mr. Thomas Horgan at the Submillimeter-Wave Technology Laboratory for their considerable efforts in the development of the radar system used to conduct this signature collection.

## REFERENCES

1. M. Davis, P.G. Tomlinson, and R.P. Maloney, "Technical challenges in ultra-wideband radar development for target detection and terrain mapping," Proceedings of the IEEE Radar Conference, 1999.
2. M.I. Mirkin, C.F. Lee, T.O. Grosch, B.E. Hedges, S. Ayasli, K. Kappra, and K. Sturgess, "Results on ground penetration SAR phenomenology from June 1993 Yuma experiment," Proceedings of the IEEE Radar Conference, 1995.
3. L.M. Ulander, W.E. Pierson, M. Lundberg, P. Follo, P. Frolind, and A. Gustavsson, "Performance of VHF-band SAR change detection for wide-area surveillance of concealed ground targets," Proceedings of the SPIE, Vol. 5427, 2004.
4. G.J. Moussally, R.W. Fries, and R. Bortins, "Ground-penetrating synthetic-aperture radar for wide-area airborne minefield detection," Proceedings of the SPIE, Vol. 5415, 2004.
5. A. Andrews, J. Ralston, and M. Tuley, "Research on Ground-Penetrating Radar for Detection of Mines and Unexploded Ordnance: Current Status and Research Strategy," Institute for Defense Analysis, IDA Document D-2416, Log: H 99-002922, 1999.
6. D.L. Schuler, J. Lee, and G. De Grandi, "Measurement of Topography Using Polarimetric SAR Images," IEEE Transactions on Geoscience and Remote Sensing, Vol. 34, No. 5, 1996.
7. L. Neng-Jing, "Radar ECCMs new area: anti-stealth and anti-ARM," IEEE Transactions on Aerospace and Electronic Systems, Vol. 31, No. 3, 1995.
8. L.M. Novak, S.D. Halversen, G.J. Owirka, and M. Hiatt, "Effects of Polarization and Resolution on the Performance of a SAR Automatic Target Recognition System," The Lincoln Laboratory Journal, Vol.8, No. 1, 1995.
9. R. Goodman, S. Tummala, and W. Carrara, "Issues in Ultra-Wideband, Widebeam SAR Image Formation," Proceeding of the IEEE Radar Conference, 1995.
10. L. Nguyen, T. Ton, D. Wong, and M. Soumekh, "Adaptive Coherent Suppression of Multiple Wide-bandwidth RFI Sources in SAR," Proceedings of the SPIE, Vol. 5427, 2004.

11. C.J. Beaudoin, "Development of a  $1/35^{\text{th}}$  Scale VHF/UHF Far-Field RCS Imaging System Used to Investigate Scattering and Imagery of Tree Obscured Targets," M.S. Thesis, University of Massachusetts Lowell, 2001.
12. M. J. Coulombe, T. Horgan, J. Waldman, J. Neilson, S. Carter, and W. Nixon, "A 160 GHz Polarimetric Compact Range for Scale Model RCS Measurements," Antenna Measurements and Techniques Association (AMTA) Proceedings, Seattle, WA, 1996.
13. M. J. Coulombe, T. Horgan, J. Waldman, G. Szatkowski, and W. Nixon, "A 520 GHz Polarimetric Compact Range for Scale Model RCS Measurements," Antenna Measurements and Techniques Association (AMTA) Proceedings, 1999.
14. T. M. Goyette, J. C. Dickinson, J. Waldman, W. E. Nixon, and S. Carter, "Fully Polarimetric W-band ISAR Imagery of Scale-Model Tactical Targets Using a 1.56 THz Compact Range," Proceeding of SPIE 15<sup>th</sup> Annual Inter. Symp. on Aerospace/Defense, Simulation, and Controls, Vol. 4382, 2001.
15. A. J. Gatesman, T. M. Goyette, J. C. Dickinson, J. Waldman, J. Neilson, and W. E. Nixon, "Physical scale modeling the millimeter-wave backscattering behavior of ground clutter," Proceeding of the SPIE, Vol. 4370, 2001.
16. R. H. Giles, A. J. Gatesman, J. Fitz-Gerald, S. Fisk, and J. Waldman, "Tailoring Artificial Dielectric Materials at Terahertz Frequencies," The Fourth International Symposium on Space Terahertz Technology, 1993.
17. C.V. Jackowatz, D.E. Wahl, P.H. Eichel, D.C. Ghiglia, and P.A. Thompson, *Spotlight Synthetic Aperture Radar: A Signal Processing Approach*, Kluwer Academic Publishers, Boston, 1996.
18. D.L. Mensa, *High Resolution Radar Cross-Section Imaging*, Artech House, Inc., Massachusetts, 1991.
19. C. Beaudoin, A. Gatesman, M. Clinard, J. Waldman, R. Giles, and W. Nixon, "Physical Scale Modeling of VHF/UHF SAR Collection Geometries," Proceedings of the IEEE Radar Conference, 2004.
20. K.W. Forsythe and A.F. Yegulalp, "Waveforms, Signal Processing and Performance of Sparse-Band Synthetic Aperture Radar," MIT Lincoln Laboratory, Project Report FPR-15, 2001.

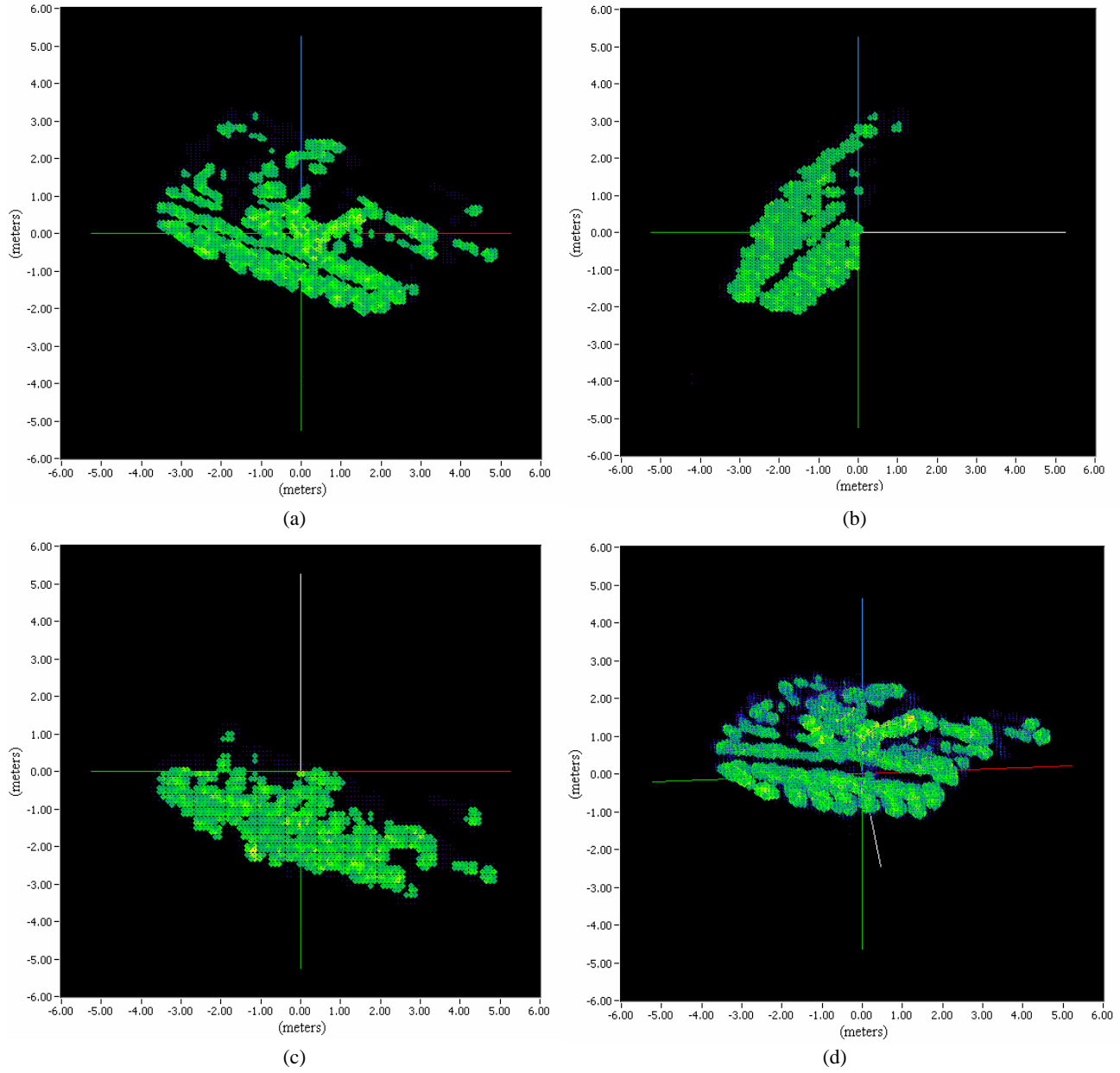


Figure 4: 3D UHF VV ISAR imagery of the M1A1 Abrams MBT at  $\theta_c = 120^\circ$ ,  $\psi_c = 45^\circ$ :  
 (a)  $x$ - $z$  (front) projection (b)  $y$ - $z$  (side) projection (c)  $x$ - $y$  (top) projection and (d)  
 arbitrary projection at azimuth =  $5^\circ$  elevation =  $-30^\circ$  referenced to the radar-  
 fixed coordinate system.

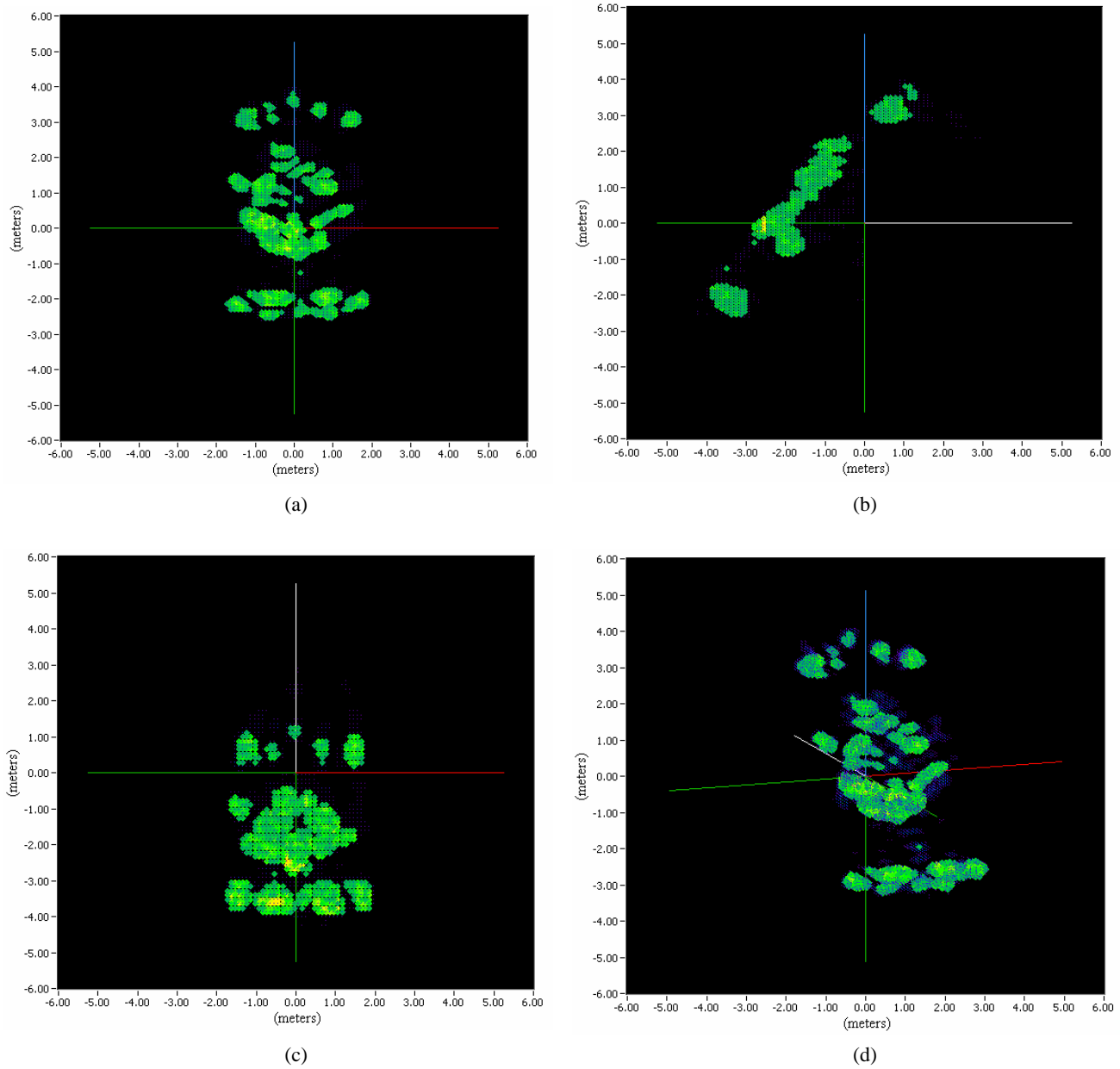


Figure 5: 3D UHF VV ISAR imagery of the M1A1 Abrams MBT at  $\theta_c = 180^\circ$ ,  $\psi_c = 45^\circ$ :  
(a)  $x$ - $z$  (front) projection (b)  $y$ - $z$  (side) projection (c)  $x$ - $y$  (top) projection and (d)  
arbitrary projection at azimuth =  $-20^\circ$  elevation =  $15^\circ$  referenced to the radar-  
fixed coordinate system.